

Personalized virtual-heart technology for guiding the ablation of infarct-related ventricular tachycardia

Adityo Prakosa^{1,7}, Hermenegild J. Arevalo^{1,2,7}, Dongdong Deng^{1,7}, Patrick M. Boyle¹, Plamen P. Nikolov¹, Hiroshi Ashikaga³, Joshua J. E. Blauer⁴, Elyar Ghafoori⁴, Carolyn J. Park¹, Robert C. Blake III¹, Frederick T. Han⁵, Rob S. MacLeod⁴, Henry R. Halperin³, David J. Callans⁶, Ravi Ranjan⁴, Jonathan Chrispin³, Saman Nazarian⁶ and Natalia A. Trayanova^{1,3*}

Ventricular tachycardia (VT), which can lead to sudden cardiac death, occurs frequently in patients with myocardial infarction. Catheter-based radio-frequency ablation of cardiac tissue has achieved only modest efficacy, owing to the inaccurate identification of ablation targets by current electrical mapping techniques, which can lead to extensive lesions and to a prolonged, poorly tolerated procedure. Here, we show that personalized virtual-heart technology based on cardiac imaging and computational modelling can identify optimal infarct-related VT ablation targets in retrospective animal (five swine) and human studies (21 patients), as well as in a prospective feasibility study (five patients). We first assessed, using retrospective studies (one of which included a proportion of clinical images with artefacts), the capability of the technology to determine the minimum-size ablation targets for eradicating all VTs. In the prospective study, VT sites predicted by the technology were targeted directly, without relying on prior electrical mapping. The approach could improve infarct-related VT ablation guidance, where accurate identification of patient-specific optimal targets could be achieved on a personalized virtual heart before the clinical procedure.

Ventricular tachycardia (VT), a life-threatening fast heart rhythm, occurs frequently in patients with myocardial infarction and can lead to sudden cardiac death. Catheter-based radio-frequency ablation, which delivers energy to destroy the ability of cardiac tissue to conduct electrical signals, offers the possibility of a permanent cure as it disrupts the propagation of abnormal electrical waves sustaining VT. However, eliminating infarct-related VT with ablation has achieved only modest success, at rates of around 50–88%^{1,2}. This stems from limitations in current techniques for mapping the electrical functioning of the heart and identifying targets for ablation. These include limited spatial sampling during mapping, with resolution often insufficient to identify critical VT propagation pathways^{3–5}, haemodynamic intolerance during the VT ablation procedure, and ambiguities in correlating electrical maps with heart anatomy⁶. Furthermore, the complex 3D pathways of cardiac impulse propagation around/through the zone of infarct during VT are often difficult to reconstruct by mapping the ventricular surfaces only^{7,8}. These limitations could translate into inaccurate ablation targets and extensive lesions, and could prolong the duration of the procedure (4–12 h), potentially increasing the risk of complications and radiation overexposure^{9,10}.

Here we present the proof of concept of a ‘virtual heart’ methodology for determining the optimal targets for infarct-related VT ablation that completely eliminates the need for invasive electrical mapping. We call this non-invasive approach ‘virtual-heart

arrhythmia ablation targeting’ (VAAT). The approach is based on cardiac imaging and computational modelling, and is personalized to each patient. Similarly to our previously developed ‘virtual-heart arrhythmia risk prediction’ (VARP) approach¹¹ for stratifying patients at risk of sudden cardiac death, the new VAAT technique involves constructing 3D computer models of patients’ hearts (ventricles) from clinical magnetic resonance imaging (MRI) data and executing simulations to evaluate the patient-specific VTs. In the current study, the virtual-heart simulation strategy is further developed and applied in a different clinical arena: the non-invasive planning and guidance of the clinical procedure of VT ablation. With the VAAT approach, once all patient-specific VTs are evaluated, we determine automatically (using an algorithm) the optimal ablation targets that render, with minimum lesion size, each heart not inducible for VT from any ectopic site. In a significant departure from all current VT ablation procedures, the VAAT approach targets termination not only of VTs that are clinically manifested or induced at the time of procedure, but of all VTs that could arise from the given post-infarction substrate, including those that might arise following initial ablation, thus potentially eliminating the need for repeated ablations and offering long-term freedom from VT. In addition to automatically determining the ablation targets, VAAT overcomes significant additional technical challenges in combining virtual-heart output with the clinical electroanatomical navigation system, and represents the first direct integration of computational modelling in cardiac patient care.

¹Institute for Computational Medicine and Department of Biomedical Engineering, Johns Hopkins University, Baltimore, MD, USA. ²Cardiac Modelling Department, Simula Research Laboratory, Fornebu, Norway. ³Division of Cardiology, Department of Medicine, Johns Hopkins University School of Medicine, Baltimore, MD, USA. ⁴Department of Bioengineering, University of Utah, Salt Lake City, UT, USA. ⁵University of Utah Health Sciences Center, Salt Lake City, UT, USA. ⁶Department of Medicine, University of Pennsylvania, Philadelphia, PA, USA. ⁷These authors contributed equally: Adityo Prakosa, Hermenegild J. Arevalo, Dongdong Deng. *e-mail: ntrayanova@jhu.edu

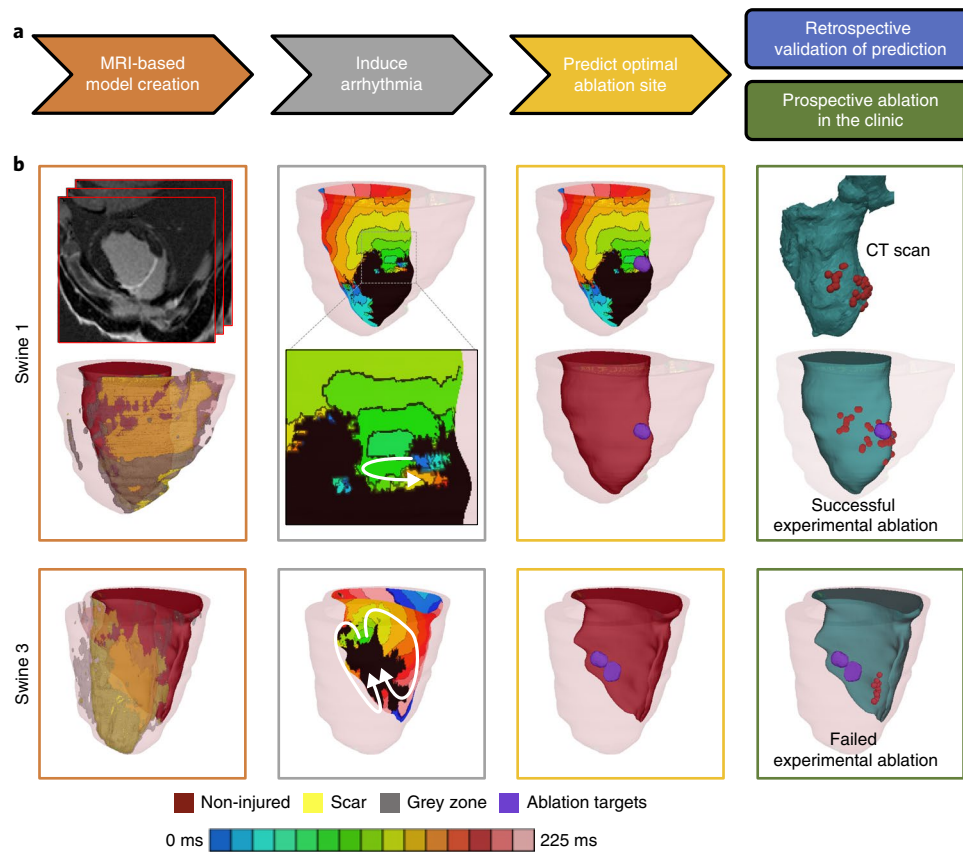


Fig. 1 | The VAAT protocol and results from the animal study. **a**, A flowchart summarizing the protocol (arrowed steps) and the retrospective and prospective studies. **b**, In silico models and predictions for one case of successful mapping-guided ablation in swine 1 (top), and one case of failed mapping-guided ablation in swine 3 (bottom). Columns, left to right: reconstructed ventricular model with different remodelled regions (with the top panel showing the LGE-MRI stack for swine 1); endocardial electrical activation maps of the infarct-related VTs, with white arrowheads showing the direction of propagation of the excitation wave, and the inset in the top panel showing the zoomed-in propagation waves through channels in the scar in swine 1; purple circles correspond to in silico predicted ablation targets on the ventricular endocardial surface; CARTO XP ventricular geometry from post-ablation CT scans co-registered with the MRI-based model for comparison of the predicted ablation targets with experimental mapping-based endocardial ablation locations, where red dots correspond to location of the catheter during ablation. The panel frame colours correspond to the protocol steps outlined in **a**. Non-injured, scar and grey zone tissues and VAAT ablation targets are shown in red, yellow, grey and purple respectively. The colour scale indicates activation times for column 2; black indicates tissue regions that did not activate.

Described in the paper are the animal ($n = 5$) and human ($n = 21$) retrospective studies, and the proof-of-concept prospective patient study ($n = 5$), that illustrate the utility of VAAT to non-invasively determine the optimal ablation targets.

Overview of VAAT

The arrowed steps in Fig. 1a summarize the VAAT method, as we envision it for guidance of the clinical procedure of infarct-related VT ablation. First, an individualized geometric model of the post-infarction ventricles is reconstructed from late-gadolinium-enhanced (LGE)-MRI, as previously described^{11,12}, with representations of both scar and infarct border zone (termed the grey zone). Determining the personalized fibre orientations using a validated approach¹³ completes geometric reconstruction. Region-specific cell and tissue electrical properties are then assigned to the geometric model. To determine all VT reentrant pathways that the infarct-remodelled ventricular substrate can sustain, we conduct a virtual multi-site delivery of electrical stimuli (pacing) from a number of bi-ventricular locations, each attempting to elicit VT from a site positioned differently with respect to the infarct. The methodology for evaluating the VTs in post-infarction heart models has been previously presented and validated in an arrhythmia risk prediction clinical study involving 41 patients¹¹.

The next step in the VAAT method determines the minimum-size (optimal) ablation lesions in each personalized virtual heart that render it no longer inducible for VT from any pacing location. These optimal targets are determined using an automatic algorithm we developed recently¹⁴. The algorithm represents reentrant wave propagation associated with each of the inducible VTs in the given heart model as a flow network, and identifies the smallest amount of tissue that, when eliminated from the network, disrupts and terminates the flow. The algorithm was validated in a retrospective study in patients with atypical atrial flutter¹⁴, and this is its first application to ventricular arrhythmias.

Once the VAAT ablation lesions are calculated, they are incorporated back in the corresponding virtual-heart model and the VT inducibility protocol is repeated to assess whether VT is inducible from any of the pacing sites. Should a new VT arise in the modified-by-ablation ventricular substrate, the VAAT protocol is repeated until complete VT non-inducibility is achieved. The resulting set of ablation lesions represents the targets that will be directly approached during the clinical procedure, without any electrical mapping. The set of VAAT ablation lesions is expected to result in the complete elimination of the ability of the infarct-remodelled ventricular substrate to sustain VT.

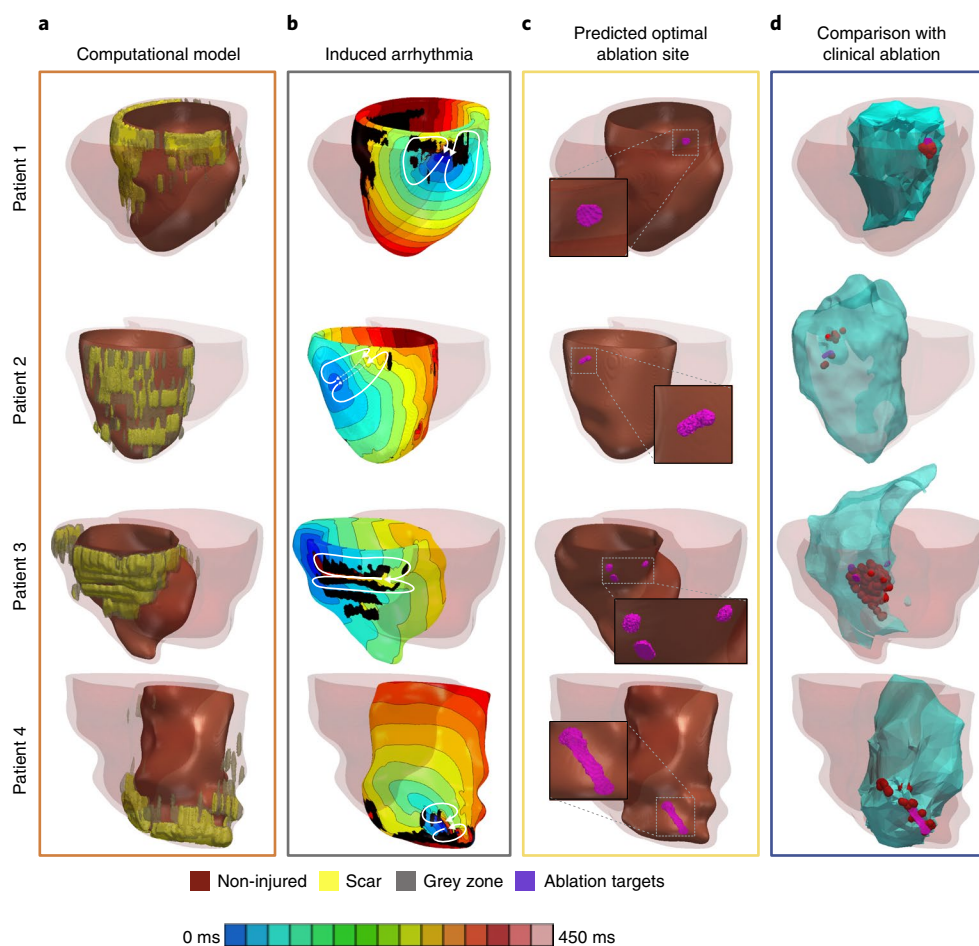


Fig. 2 | Results from the retrospective human study. Representative examples of *in silico* models and predictions from four patients are shown. **a**, Reconstructed ventricular computational model with different structurally remodelled regions. **b**, Electrical activation maps of the infarct-related VTs after induced arrhythmia on the epi- or endocardial surfaces. The white arrowheads show the direction of propagation of the excitation wave. The colour scale indicates activation times and black indicates tissue regions that did not activate. **c**, The purple regions correspond to VAAT-predicted ablation targets on the endocardial surface, and insets show the zoomed-in VAAT predictions. **d**, Co-registration of VAAT targets with the CARTO 3 endocardial surface (blue) showing clinical ablation. The red dots correspond to locations of the tip of the catheter during ablation. Non-injured, scar and grey zone tissues and VAAT ablation targets are shown in red, yellow, grey and purple, respectively.

In the prospective study, VAAT is executed during the brief time interval between the acquisition of patient MRI and the clinical ablation procedure (<24 h). Once calculated, the set of predicted ablation targets are exported, then uploaded and co-registered in the clinical electroanatomical navigation system before the procedure commences.

A full description of the VAAT methodology is provided in the Methods.

VAAT proof-of-concept studies

The capability of VAAT to non-invasively determine the ablation targets that eliminate all infarct-related VTs with minimum lesions was illustrated in retrospective and prospective studies (Fig. 1a).

A retrospective animal study (swine model, $n = 5$) showed that VAAT is able to reproduce successful mapping-based ablation outcomes but with reduced lesion size, and provides superior targets when mapping-based ablation failed. For the two cases of successful experimental ablation (swine 1 and 2; Fig. 1b top and Supplementary Fig. 1, respectively), VAAT lesions were in the same regions as experimental lesions (red dots mark the ablation catheter tip, visible in computed tomography (CT) scans), highlighting the predictive capability of the virtual-heart approach. Analysis of post-ablation MRI scans showed significant difference in lesion volumes

between experiment and VAAT (swine 1, 0.39 cm^3 vs 0.19 cm^3 ; swine 2, 0.37 cm^3 vs 0.28 cm^3). In the remaining animals (swine 3 to 5, Fig. 1b bottom and Supplementary Fig. 1), mapping-based lesions that failed to terminate VT were located away from the locations of the VAAT targets that eliminated the VTs (see Supplementary Table 1 for simulated lesion volumes).

Two retrospective human studies ($n = 21$ total) in patients that had undergone pre-procedure LGE-MRI and successful infarct-related VT ablation were then undertaken to demonstrate that VAAT lesions fall within the areas ablated clinically. The first study was in patients without implantable cardioverter defibrillator (ICD) devices ($n = 16$). Four cases are shown in Fig. 2 and another 10 are presented in Supplementary Fig. 2. Fig. 2 (third and fourth columns) shows that in patients 2–4, the predicted lesions (see Supplementary Table 2 for calculated lesion sizes in all 16 patients) were smaller than the clinical lesions (compared to the extent of endocardial surface enclosing ablation catheter tip locations in the electroanatomical navigation (CARTO) maps; each lesion is of typical size¹⁵: $6.7 \times 9.4 \times 3.4 \text{ mm}^3$, that is, 0.21 cm^3).

Since the majority of patients who undergo infarct-related VT ablation have ICDs, which impose image artefact, we conducted a second human retrospective study ($n = 5$) to assess the feasibility of determining the optimal infarct-related VT ablation targets

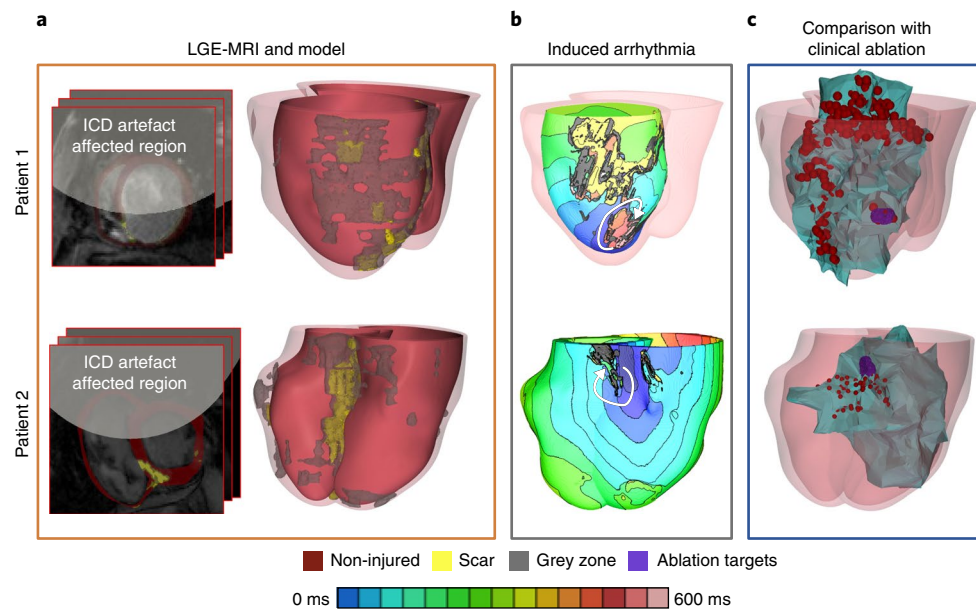


Fig. 3 | Results from the retrospective human study in patients with ICDs. Representative examples of in silico models and predictions from two patients. The myocardial wall artefact burden was 59% and 46% for patients 1 and 2, respectively. **a**, LGE MRI scans with ICD artefact burden and reconstructed ventricular models with different remodelled regions. **b**, Electrical activation maps of the infarct-related VTs on the epi- or endocardial surfaces (chosen for best visualization). White arrowheads indicate the direction of VT propagation. The colour scale indicates activation times and black indicates tissue regions that did not activate. **c**, Co-registration of ventricular model surfaces and the VAAT ablation targets (purple) with the CARTO endocardial surfaces (blue) showing clinical ablation locations corresponding to red dots representing locations of the tip of the catheter during ablation. The CARTO endocardial surfaces show the left ventricle for patient 1 and the right ventricle for patient 2 co-registered with the corresponding MRI shells obtained in the corresponding individuals at the time of their clinical procedure. In patient 1, the predicted ablation target overlapped with the clinical lesions at the same location. The clinical ablation also identified extensive lesions at the periphery of the infarct (the grey zone). In patient 2, the VAAT lesion was within the area ablated clinically. Non-injured, scar and grey zone tissues and VAAT ablation targets are shown in red, yellow, grey and purple, respectively.

in patients with ICDs despite the artefact burden, thus broadening the clinical utility of the VAAT approach. For this purpose, we developed an enhanced model generation methodology (see Methods and Supplementary Fig. 3) applicable for cases where the ICD artefact did not cover the LGE regions. Of the five randomly selected patients with ICDs, two had a negligible myocardial artefact burden, while in the remaining three the artefact ranged from 46 to 62%. LGE regions indicative of infarct-related structural remodelling were identifiable outside of the ICD artefact in all five cases. In this retrospective study, simulations were conducted blind to the clinical data. For all patients, targets predicted by VAAT generally corresponded to clinical lesions (Fig. 3 presents the ablation results for two patients, with Supplementary Video 1 showing VT in one; the rest are shown in Supplementary Fig. 4), but were smaller in size; myocardial burden artefacts and simulated lesion sizes are presented in Supplementary Table 3. Note that in patient 1, the clinical ablation lesion known in this case to have resulted in acute VT termination and the VAAT lesion fully coincided. In this patient's clinical procedure, the infarct scar was additionally encircled with lesions targeting the grey zone in an attempt to prevent VT recurrence; VAAT demonstrated that this lesion was sufficient to eliminate the arrhythmogenic propensity of infarct substrate. This retrospective patient study showed that despite the ICD artefact, in cases when the ICD artefact does not obscure the zone of infarct, the VAAT approach could non-invasively predict the optimal VT ablation targets and thus be used to guide clinical ablation.

We next embarked on a prospective human study ($n = 5$) at two different clinical centres, the University of Utah (three patients,

January 2015 to December 2016) and the University of Pennsylvania (two patients, November to December 2017), to assess the feasibility of VT ablation that directly targets sites predicted by the VAAT approach, without prior intracardiac mapping. The prospective study also served to determine whether the VAAT protocol could be executed within the relevant clinical timeframe.

Figure 4 presents two cases, one from each clinical centre, of successful VAAT-guided ablations in a post-infarction patients with inducible sustained VT. Model-generated ventricular images with the VAAT targets were imported into the clinical electroanatomical navigation system (Fig. 4), so that the ablation catheter could be directly steered towards the targets. After ablation of the VAAT targets, a clinical VT inducibility pacing protocol (see Methods for details on the clinical protocol) was executed to confirm that VT was no longer inducible. Activation maps of the two VT morphologies in a Utah patient are shown in Fig. 4b, and Supplementary Fig. 5 and Supplementary Video 2 present transmembrane potential maps over time for one of the two induced VT morphologies in this patient. The patient has since remained VT-free, over the 23-month follow-up period. Similarly, in another patient at the same centre, VT was also inducible, and the VAAT-predicted sites were directly ablated. However, the patient went into ventricular fibrillation following the procedure and had to be cardioverted. Nonetheless, following the VAAT-driven ablation, the patient has since remained VT-free, over the follow-up period of 21 months. In the third patient, despite the presence of scar tissue on the MRI, the model predicted that VT would not be inducible. This matched the clinical outcome, as infarct-related VT was indeed not inducible during the electrophysiological study despite the patient's history of myocardial

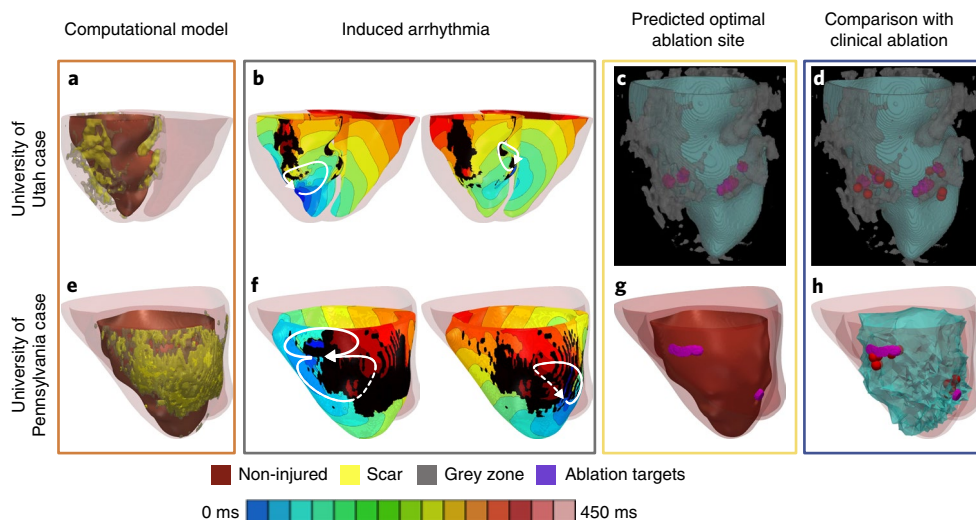


Fig. 4 | Results from the prospective human study. a–h, VAAT-guided ablation for a patient at the University of Utah (**a–d**) and another at the University of Pennsylvania (**e–h**). **a,e**, Reconstructed ventricular models with different remodelled regions. **b,f**, Activation maps corresponding to the two VT morphologies induced in the Utah and Pennsylvania patient models, respectively. White arrowheads depict the direction of propagation of the excitation wave. The colour scale indicates activation times and black indicates tissue regions that did not activate. **c,g**, VAAT-predicted ablation targets for the two VT morphologies. **d,h**, Co-registration of the VAAT-predicted targets (purple) with the CARTO 3 endocardial surface (green). The red dots correspond to locations of the tip of the catheter during ablation. The left ventricular endocardial surface is shown in green and the total infarct region is shown in grey. Non-injured and scar tissues are shown in red and yellow, respectively.

infarction; instead, the sustained wide-complex tachycardia was found to be supra-ventricular tachycardia with aberrancy.

Among the two prospective patients undergoing ablation at the University of Pennsylvania, one was not inducible for VT in the clinic. VAAT predicted VT non-inducibility before the clinical procedure; the model was not inducible for VT despite the presence of scar tissue/grey zone. In the other patient, the VAAT targets were successfully ablated and VT terminated. Two VT morphologies in this patient are shown in Fig. 4f, with targets in Fig. 4g, and co-registration of VAAT targets and ablation catheter tip locations during the procedure (Fig. 4h). The prospective human studies demonstrated that a simulation-driven VT ablation procedure is feasible within the clinical workflow and timeline, and that it can be executed at different clinical centres.

Discussion

This study presents VAAT, a virtual-heart approach to predict the optimal targets for infarct-related VT ablation. The approach could eliminate the need for invasive electrical mapping during the clinical procedure. VAAT determines the ablation targets non-invasively, on the basis of a comprehensive evaluation of all 3D VT reentrant circuits that the infarct-remodelled substrate can support. The targets are calculated by an algorithm that determines the minimum amount of tissue that, when rendered non-excitable, eliminates all VTs—not only those manifested clinically or induced during the procedure, but also those VTs that could arise if the arrhythmogenic propensity of the substrate was not fully eliminated during the initial ablation. The VAAT approach could thus have the potential to not only guide infarct-related VT without prior electrical mapping, but to also eliminate the need for repeated ablations, offering long-term freedom from VT.

Here we describe the conceptual underpinning of the approach, and present comparisons of VAAT lesions with retrospective experimental (5 animals) and clinical (21 patients) ablation lesion data. As the lesion data are retrospective, and represents information about all lesions inflicted during the clinical procedure, such a comparison serves to primarily demonstrate VAAT lesion location correspondence and lesion size advantage. The promising results from

the proof-of-concept prospective studies (5 patients) at two clinical centres demonstrate the feasibility of conducting a large prospective patient study, and underscore the VAAT potential for translation to the clinic for guidance of VT ablation in patients. Should the capability of the VAAT approach be demonstrated in such prospective studies, VAAT holds the promise to radically change infarct-related VT ablation, engendering swift and precise delivery of ablation without prior electrical mapping, and eradicating all possible VTs the substrate can sustain, thus eliminating or at least reducing the need for redo procedures. This could result in a dramatic improvement in the efficacy of and tolerance for the therapy, as well as in the reduction of post-procedure complications. Finally, since early use of VT ablation post-infarction has been shown to result in much improved patient outcomes (SMASH-VT trial)¹⁶, an accurate and easily executed VT ablation will lead to significant widening of the therapeutic potential of the procedure: the latter could become first-line therapy for infarct-related VT, in contrast to its current use only after drugs have failed.

Notably, the VAAT approach bypasses the need to establish the entity targeted by ablation, whether the latter is a channel in the scar^{17,18}, part or all of the grey zone¹⁹ or one or more reentrant drivers²⁰. Additional utility of the approach is derived from the fact that it could inform the operator whether the approach to the target(s) is endo- or epicardial, as these require different anticoagulation set-ups, thus providing additional money and time savings, and decreasing radiation and associated complications. Importantly, since the predicted targets are 3D, they may not always be fully reachable via an endo- or epicardial approach; in such cases, we envision re-computing the targets, taking into account that a given portion of the initial predicted target will need to remain excitable.

The VAAT approach could be extended²¹ to the rapidly increasing population of patients with non-ischaemic cardiomyopathy, where myocardial structure incorporates distributed fibrosis/scar tissue, and to patients with arrhythmias secondary to surgical repair in congenital heart disease, such as Tetralogy of Fallot. Furthermore, since VAAT is based on a simulation method representing processes from the molecular to the whole organ, it could be potentially modified to input patient-specific genetic and

pathophysiological data, and thus its application could be broadened to arrhythmias arising from cardiac diseases of various aetiologies. Integrating image-based computational modelling into treatments for heart rhythm disorders could thus advance personalized approaches to heart disease.

Methods

MRI datasets and experimental protocol of the retrospective animal study. The retrospective animal study (swine model, $n = 5$) was conducted to demonstrate that the VAAT methodology was able to reproduce successful mapping-based ablation outcomes but with reduced target size, and to provide superior alternative targets when mapping-based ablation failed. The details of both *in vivo* MRI acquisition and the electrophysiology study (EPS) in these animals have been previously described²². In brief, myocardial infarction was induced via occlusion of the mid-left anterior descending coronary artery. All animals were ~2 months old, with weight ranging from 18–23 kg, and 2/5 were male. Four weeks after occlusion, high-resolution *in vivo* cardiac MRI (3.0-T scanner, Achieva, Philips Medical Systems) with LGE was acquired at a resolution of $976 \times 976 \times 4,000 \mu\text{m}^3$. A CT scan was also acquired. One day after image acquisition, the animals underwent a traditional EPS with intracardiac mapping to determine the infarct-related VT targets and perform ablation guided by the CARTO XP electroanatomic mapping system (Biosense Webster). Seven to nine days post-ablation, a follow-up EPS was conducted to determine if ablation resulted in VT non-inducibility. In two of the five swine hearts, ablation succeeded and VT remained non-inducible; in the other 3, ablation failed. A post-ablation *in vivo* LGE-MRI was also performed at that time to document the actual extent of the ablation lesions.

Clinical MRI datasets and protocols of the retrospective patient studies. Both human retrospective studies ($n = 21$ total), with and without ICDs, included patients whose pre-ablation cardiac LGE-MRI showed myocardial scar tissue (on a 1.5-T scanner, Avanto, Siemens Medical Solutions; resolution $\sim 1.5 \times 1.5 \times 10.2 \text{ mm}^3$). All the patients underwent the standard EPS (voltage and pace mapping) to determine the locations of the ablation targets and (successful) ablation of the infarct-related VTs under the guidance of a CARTO 3D electroanatomical mapping system. Radiofrequency ablations were performed at the target regions during sinus rhythm. If non-clinical VT morphologies were inducible, those were also ablated; all the clinical ablation lesions executed during each procedure are shown in the corresponding figures. After completing ablation, programmed stimulation was repeated to determine inability to induce VT. Acute success was defined as the inability to induce clinical VT at the end of the procedure.

The first human retrospective study involved 16 patients, all without ICDs (so that myocardial wall was not obscured in MRI), with the aim to compare the VAAT targets with the clinical lesions and determine whether the VAAT prediction fell within the areas ablated clinically. Eight of these patients were referred for catheter ablation of VT at the Johns Hopkins Hospital in the period between July 2006 and April 2013; the MRI data used in this study have been previously published²³. The mean patient age in this retrospective study was 64.4 ± 9 years, the mean left ventricular ejection fraction (LVEF) was $38.4 \pm 12\%$, and the cohort was 87.5% male. The other 8 patients were referred for catheter ablation of VT also at the Johns Hopkins Hospital in the period between November 2010 and October 2017; their MRI data have not been used for model reconstruction in any previous study. Results from 4 of these patients are shown in Fig. 2. The mean patient age in this group was 64.1 ± 15.5 years, the mean LVEF was $31.1\% \pm 16.4\%$, and the cohort was 75% male.

In the second retrospective study, 5 patients with ICDs were chosen randomly to demonstrate that VAAT could also be used to predict ablation targets in such patients; these patients were referred for catheter ablation of VT at the Johns Hopkins Hospital between December 2010 and November 2013. The mean patient age was 54.2 ± 9.3 years, the mean LVEF was $39 \pm 13.8\%$, and the cohort was 100% male. ICD artefact burden in the MRIs of these patients ranged from 0–62% of myocardial volume but did not cover the LGE regions (see the main text for details).

For clarity, in this paragraph we reproduce parts of the section on 'EPS and ablation' from our previously published paper²³. All patients underwent the standard EPS and ablation of scar-related VT under the 3D CARTO guidance during sinus rhythm. After ablation, programmed stimulation was repeated. Acute success was defined as the inability to induce clinical VT at the end of the procedure. If non-clinical VT morphologies were inducible, those were also ablated.

The Johns Hopkins Institutional Review Board (IRB) approved sharing of de-identified patient data with the modelling team for the retrospective study. Given the retrospective nature of the study, the IRB did not require patient informed consent.

Prospective patient study. The prospective study enrolled patients with infarct-related VT at the University of Utah and the University of Pennsylvania with the goal to demonstrate feasibility of using the non-invasive VAAT approach to guide clinical ablation. All patients had VT, and were referred for ablation; they

all underwent LGE-MRI. At the University of Utah, three patients were targeted for ablation between January 2015 and December 2016. The mean patient age was 66.6 ± 9.9 years, the mean LVEF was $40 \pm 6.6\%$, and 2/3 patients were male. At the University of Pennsylvania, two patients were targeted for ablation between October and December 2017. The mean patient age was 73.5 ± 3.4 years, the mean LVEF was $33 \pm 4.4\%$, and the cohort was 100% male.

At both clinical centres, during the ablation procedure VT was induced by programmed electrical stimulation. VAAT-predicted ablation site(s) were then imported in CARTO (see below for import and merger methodology details). Ablation was then targeted to these sites using an irrigated thermocool ablation catheter. After ablation, VT non-inducibility was verified by repeating programmed electrical stimulation. The protocol was approved by the Institutional Review Boards of the University of Utah Health Sciences Centre and the Hospital of the University of Pennsylvania. All patients enrolled gave informed consent.

VAAT approach. Heart structural model construction. Both animal and human models of 3D ventricular structure were reconstructed from the cardiac LGE-MRI data. The procedure is described in full detail in our recent publication on arrhythmia risk stratification in patients with myocardial infarction¹¹. Briefly, for each heart, the myocardial boundaries in the MRI stack were contoured and the 3D ventricular wall geometry was reconstructed using a method based on variational implicit functions interpolation used previously by our team and validated with clinical data¹². To represent the geometry of the infarct in each ventricular geometrical model, myocardial regions were classified as infarcted and non-infarcted areas by means of signal thresholding¹¹. Each infarct region was further classified into scar and grey zone tissue using a full-width half-maximum (FWHM) approach that has been validated previously²⁴. The 3D geometries of the infarct zones were reconstructed and merged with the corresponding ventricular geometry reconstruction.

Construction of ventricular models from LGE-MRI scans of patients with ICDs involved additional processing steps to overcome the presence of artefact in the image. Following segmentation of the ventricular wall portion unobstructed by the shadow, we extrapolated the ventricular boundaries into the area occluded by the ICD artefact. Within the reconstructed ventricular wall, myocardium covered by the ICD shadow was delineated from unobstructed myocardium on the basis of the 3D radial distance from the ICD (Fig. 3 and Supplementary Figs. 3 and 4). Outside of the shadow, standard image processing classified the myocardium as non-infarcted, scar or grey zone tissue, based on pixel intensity, as described above. The ventricular wall within the region of ICD shadow was assumed to have non-infarcted tissue properties, as it was outside of the zone of infarct. The burden of ICD artefact in the ventricular wall in each of the 5 patients is presented in Supplementary Table 3.

Generating the computational meshes and assigning fibre orientation. For both animal and human heart models, finite-element ventricular meshes were generated as described previously^{11,25,26}, with an average resolution of $350 \mu\text{m}$; ventricular models thus comprised of ~4 million nodes. The choice of finite element size was dictated by the need to resolve wavefront propagation in the simulations while simultaneously minimizing computational expense^{11,27,28}.

Finally, fibre orientations, specific to the individual geometry of the ventricles, were assigned to each ventricular computational mesh on a per-element basis (as in our previous publications^{11,26,29}) using an efficient rule-based approach that we developed and validated¹³. This fibre orientation methodology uses the Laplace–Dirichlet method to define transmural and apicobasal directions at every point in the patient-specific ventricles. It then employs bi-directional spherical linear interpolation to assign fibre orientations based on a set of fibre orientation properties (rules). After fibre orientation was assigned to the elements in the ventricular mesh, the corresponding 'masks' of infarct scar and grey zone tissue were superimposed. Additional detail can be found in our recent publication¹¹.

After fibre orientations were assigned, the corresponding grey zone and scar 'masks' are superimposed. Grey zone fibre orientations did not incorporate any changes in fibre orientation in that region (although there are changes in grey zone conductivity and anisotropy; see below). The justification of this representation is based on a recent study³⁰ that used sub-millimetre-resolution diffusion tensor and LGE-MRI on a clinical scanner to examine the detailed organization of the infarct structure in the ventricles. The study demonstrated preservation of primary eigenvector (fibre) orientation at the thinned region of infarct in both human and porcine hearts.

Altogether, reconstruction of each patient heart took up to 8 h.

Electrophysiological modelling. Details regarding electrophysiological modelling in the swine hearts can be found in our recent paper²⁹. Details on all aspects of human ventricular electrophysiological modelling in myocardial infarction is presented in another of our recent publications¹¹. Briefly, for all heart models, both animal and human, once the 3D finite-element ventricular mesh was generated, regionally-uniform cell and tissue electrophysiological properties were assigned to the three regions outlined in the virtual heart from the LGE-MRI scans: scar, grey zone and non-infarcted tissue. All finite elements that belonged to the scar region were considered electrically non-conductive. In the patient-specific heart models, finite

elements that belonged to non-infarcted tissue and grey zone were assigned human ventricular cell action potential dynamics²¹; a different action potential model was used in the animal study²⁹. Modifications to the ionic model based on experimental recordings were implemented to represent electrophysiological remodelling in the grey zone^{11,29}. Overall, the grey zone action potentials were characterized by a longer duration, decreased upstroke velocity, and decreased peak amplitude compared to those in the non-infarcted myocardium, similar to what has been previously reported^{32,33}. Specifically, as described in the animal model study²³, action potential remodelling in the grey zone was implemented by decreasing the original action potential parameters as follows: peak sodium current to 38%, peak L-type calcium current to 31%, and peak potassium currents I_{Kr} and I_{Ks} to 30 and 20%, respectively. The human action potential model in the patient studies was similarly modified to represent electrophysiological remodelling in the grey zone, based on experimental data, as described in our previous patient study¹¹: 62% reduction in peak sodium current, 69% reduction in L-type calcium current and a reduction of 70 and 80% in potassium currents I_{Kr} and I_{Ks} , respectively.

Tissue properties representing animal or human ventricular cell-to-cell electrical communication were also assigned to the non-infarcted and grey zone regions, as described previously¹¹; the grey zone region was characterized by a decrease in transverse conductivity to reflect connexin-43 remodelling in the infarct border zone. Similar to the latter study, the values of the non-infarcted tissue conductivities used here were 0.255 and 0.0775 S m⁻¹ in the longitudinal and transverse directions, respectively.

Simulation of electrical activity and numerical aspects. The propagation of electrical activity in a virtual heart was simulated by solving, using the finite-element method, a reaction-diffusion partial differential equation, representing the spread of current in the ventricular myocardium, together with the ordinary differential and algebraic equations representing myocyte membrane dynamics at each node in the mesh²⁷. Simulations of electrical activity in the patient-specific heart models were executed in a monodomain representation of the myocardium using the software package CARP (Johns Hopkins University, University of Bordeaux and University of Graz) on a parallel computing system^{27,34}. The system of equations was solved with a time step of 25 μ s. Full details regarding the simulations of electrical activity in the heart models is found in our recent publication¹¹ as well as in a number of earlier publications from our team^{35–37}.

VT induction protocol. Each individualized ventricular model was subjected to pacing from multiple bi-ventricular locations in an attempt to elicit reentrant arrhythmias, thus revealing the potential of the disease-remodelled ventricles to cause degeneration of electrical signal propagation into arrhythmic activity following premature beats that originate at different locations in the heart. The protocol used here is identical to that in the VARP approach in our previous study¹¹, with the exception of the larger number of pacing sites used here. Each virtual heart was paced from 26 uniformly distributed (basal, medial, apical, lateral, septal, posterior and anterior) locations, 9 on the right ventricular endocardium, and 17 on the left ventricular (LV) endocardium, the latter one in each of the AHA LV segments³⁸. The rationale for choosing a large number of pacing sites was based on clinical studies, which have shown a positive correlation between the number of pacing sites and inducibility of ventricular arrhythmia^{39,40}. The distribution of pacing sites throughout the ventricles ensured that the protocol covered a large range of possibilities for potential sites at which ectopic foci could emerge and captured all the possible arrhythmias that could arise from the given infarct morphology, and not only the one that was clinically manifested. Further increase in the number of pacing sites did not uncover more unique VTs. All pacing sites were assigned in the model automatically using an approach described previously⁴¹.

The pacing pulse trains were the same as in our previous studies^{11,26,29} and consisted of 8 pacing stimuli (S1) at a cycle length of 600 ms for the human models and 300 ms for the swine models. A premature stimulus (S2) was delivered 250 ms after S1. If S2 did not result in the generation of reentrant arrhythmia, the S1-S2 interval was shortened, in 10 ms steps, until arrhythmia was induced or the S2 failed to capture the tissue. If arrhythmia was not induced, an additional S3, and if necessary S4, were delivered in the same fashion as S2 (initially delivered 250 ms after previous stimulus and then shortened until arrhythmia was induced or the stimulus failed to capture). In all simulations, the size of the pacing electrode was 1 × 1 × 1 mm³, injecting transmembrane current. Simulations were monitored to ensure that in each case an excitation wave was initiated and propagated away from the pacing location.

To ensure computational tractability of the study, each simulation run calculated ~7 s of electrical activity in the ventricles (corresponding to about 7 h execution time), the first 5 s of which was the pacing protocol, and the remaining 2 s represented the post-pacing period used to detect the presence of arrhythmia. Arrhythmias were considered persistent if they did not self-terminate over the 2 s period. Initial simulations analysing 5 s post-pacing activity in heart models demonstrated that arrhythmias that persisted for 2 s did not self-terminate after another 3 s. This behaviour is consistent with the deterministic nature of the model; the 7 s of total simulated activity also ensures turnaround time of <24 h per patient in the prospective human study.

Individual reentrant arrhythmia periods in the simulations here could not be compared to those of the reentrant circuits induced during mapping in the

human retrospective studies since the pacing sites in the virtual heart were at locations different from those of the clinical pacing sites. Importantly, simulations preliminary to this study demonstrated that changes in human action potential duration and conduction velocity within physiological boundaries changed the cycle length of the reentrant arrhythmia in a given heart model. However, the location of the organizing centre of the arrhythmia (often isthmus or grey-zone-anchored phase singularity²⁶) remained the same or nearly the same, as it was predominantly determined by the individual distribution of scar and grey zone. Indeed, for patient-specific models with structural remodelling, in simulations with $\pm 20\%$ of the normal magnitude of the potassium current I_{K1} or the calcium current I_{CaL} (resulting in action potential duration variation of ± 25 ms) and $\pm 30\%$ variation in tissue conductivity (resulting in conduction velocity variation of ± 10 cm s⁻¹), we found that the exact locations of the phase singularities varied only by ≤ 0.2 cm on average. These findings underscore the feasibility of ablation target prediction using patient-specific myocardial infarcted heart models reconstructed from patient LGE-MRI scans that incorporate average human electrophysiological properties (and thus do not require invasive electrophysiological measurements in the given patient for model parameter input).

Validation of the electrophysiological modelling of pacing-induced arrhythmias in the post-infarction ventricles. The approach used here to construct a model of the post-infarction ventricles by thresholding the infarct into scar and (homogeneous) grey zone tissue has been recently validated with experimental data. In a previous study²⁹, sock epicardial electrograms from infarct-related VT, obtained from *in vivo* swine hearts, were used to demonstrate that ventricular models reconstructed from MRI data of the corresponding hearts were able to predict fairly accurately the morphology of each VT reentrant circuit and its organizing centre (for example, isthmus). These results indicated that small heterogeneities in grey zone tissue and the Purkinje system, and additional regional electrophysiological heterogeneities, play a secondary role in determining inducibility and organization of VT; primary influences include the geometrical morphologies of the scar and grey zone, as well as the representation of different electrophysiological properties in non-infarcted tissue and grey zone. These findings are consistent with those published previously²⁶, which described a parameter sensitivity analysis of the grey zone model representation. That study found that the inclusion of small scar heterogeneities with density within physiological range did not alter inducibility of infarct-related VT. These studies provided the initial justification for the electrophysiological modelling approach in this study.

The virtual-heart approach used here was recently validated in a human retrospective study⁴¹ of 41 post-infarction patients who underwent ICD implantation. Patients were followed for the primary endpoint of appropriate ICD firing due to ventricular arrhythmia or cardiac death for 4.8 \pm 2.9 years. Blind to the clinical outcome, the virtual-heart approach assessed sudden cardiac death risk by determining VT inducibility in the patient-specific heart models following pacing from sites distributed throughout the left and right ventricles. The virtual heart test significantly outperformed several existing clinical metrics in predicting future arrhythmic events, validating the predictive capability of the modelling approach employed in the present study.

Finally, we are currently conducting an additional validation of our patient-specific modelling methodology in an ongoing clinical trial in patients receiving an ICD. An abstract of this study has been already published⁴².

Approach to automatically determine the optimal VT ablation targets. We developed an approach to automatically identify, based on the simulated reentrant circuits, the optimal ablation targets for each VT morphology. The methodology was recently described and validated in patient-specific models of atypical left atrial flutter (LAFL)¹⁴, including comparisons with clinical ablation lesions that terminated LAFL. For clarity, in this and the next paragraph we reproduce parts of the section 'Identification and ablation of minimum cuts in reentrant wave propagation' from one of our earlier papers¹⁴. In this approach, we represent wave propagation during each cycle of reentry as a flow network. A flow network is a mathematical graph that abstracts directional movement between interconnected objects. Interconnected objects are represented as vertices in a graph; links between adjacent pairs of vertices, where flow can pass through, are called edges; and the maximum possible flow between two adjacent vertices is termed edge capacity.

In this study, each vertex in the flow network corresponded to an element in the LGE-MRI-derived geometric model. Two vertices in the network were defined to be adjacent to each other if they (1) corresponded to elements that shared a common face and (2) if the difference in activation time between these elements was <20 ms. An edge in the flow network corresponded to the shared face between adjacent vertices. The capacity of a network edge was defined to be equal to the cross-sectional area of the corresponding face.

The 'minimum cut' (MC) in a flow network represents the number of edges that, when removed, separate the 3D network into 2 disconnected components. Here it was determined using the Boykov-Kolmogorov algorithm⁴³. The tissue that comprises each minimum cut represents the *in silico* equivalent of the minimal set of ablation lesions needed to terminate VT. *In silico* ablation was performed by rendering tissue within 1 mm of the MC non-excitabile. The VT induction protocol was then repeated to establish that VT was no longer inducible. If a new

VT arose after implementing the calculated ablation lesions, then additional targets corresponding to that VT were calculated. The protocol was repeated until VT was no longer inducible.

Examples that illustrate the advantages of the MC approach, highlighting its 3D nature, can be found in our earlier published study¹⁴ (see the supplementary material of that paper). Importantly, the use of the MC algorithm bypasses the need to establish in each patient what constitutes an ablation target, whether channels in the scar^{17,18}, part of or the entire grey zone¹⁹, or reentrant drivers²⁰. Finally, as already discussed in the main text, as the predicted targets are 3D, they may not be reachable in every patient via a particular endo- or epicardial approach; in such cases, we envision the targets to be re-calculated, taking into account that a given portion of the initial predicted target will need to remain excitable.

Merger of VAAT predicted targets with CARTO electroanatomical map in the prospective patient studies. To guide the ablation using the VAAT approach, the predicted targets had to be imported into the CARTO electroanatomical mapping system (CARTO 3, BioSense Webster) during the clinical procedure. To do so, we extracted the predicted targets from the virtual heart model on surface meshes and exported them into CARTO as virtualization toolkit (VTK) files (Kitware), ensuring that the resulting files are compatible with the CARTO system. To register the VAAT targets to the patient heart during the clinical procedure, additional landmarks from the patient's virtual heart geometric model were required for the registration process; the latter was performed with CartoMerge within the electroanatomical navigation system. The following surfaces were also extracted from the patient's virtual heart model, to serve as landmarks: left ventricular endocardium, left ventricular apex, right ventricular endocardium, epicardium and infarct surfaces. Additional surfaces segmented and used as landmarks included the aorta, the left aortic cusp and the right aortic cusp. All surfaces were exported as VTK files and imported into the CARTO system at the beginning of the clinical ablation procedure. The registration process performed with CartoMerge aligned the coordinates of the left ventricular apex and left and right aortic cusps of the model landmarks to the coordinates of the left ventricular apex and left and right aortic cusps of the surfaces created with the intracardiac ultrasound catheter during the procedure. This landmark-based registration superimposed the virtual heart model landmarks, including the VAAT targets, to those of the patient heart. This enabled the clinician to navigate the ablation catheter to the VAAT targets accurately. After the procedure, the CARTO study, which included the CARTO clinical electroanatomical surfaces and the ablation lesion locations registered to the patient's virtual heart model were exported for analysis. The exported files were converted to VTK files, and Paraview (Kitware) was used for visualization and comparison of the VAAT targets with the clinical ones.

The mean and standard deviation of the distance between the registered CARTO surface and the model LV endocardium was 5.77 ± 4.23 mm.

Uncertainty in target predictions and limitations of the VAAT approach. The VAAT strategy involves the use of personalized geometry and distribution of structural remodelling, but it is not personalized with respect to the electrophysiology of the patient. We use the same pre-determined 'average' electrophysiology modelling to represent non-infarcted tissue and grey zone in all of our patient-derived models. An ideal option would be to use personalized electrophysiology in each model, however acquisition of such personalized information would most likely be invasive, in contrast to the VAAT approach, which offers a non-invasive prediction of the ablation targets. Thus, the VAAT-predicted ablation targets have a level of uncertainty associated with the fact that pre-determined electrophysiology is used. One could potentially endeavour to re-calculate, as part of the VAAT workflow, the predicted patient-specific ablation targets with different pre-determined electrophysiology and then examine the differences in the resulting targets, if any. However, this is currently impossible within the clinical workflow, because of the short time window to conduct the simulations, that between clinical LGE-MRI acquisition and the ablation procedure; hospital workflow necessitates cardiac MRI acquisition the day before procedure. The issue is further exacerbated by the fact that as part of VAAT, in silico ablation with the predicted targets is also conducted and the model paced again from all pacing sites to examine VT inducibility—this procedure is repeated until the substrate is non-inducible for VT. Thus, to be able to predict the VT ablation targets non-invasively and as part of the clinical workflow, the use of pre-determined electrophysiology, with its potential uncertainty (different for each patient), will need to be retained.

In VAAT, this potential uncertainty is compounded with that associated with co-registration of predicted targets and CARTO images, as described in the previous section. Other limitations of the approach include the fact that clinical LGE-MRI quality could be operator-dependent and thus could include uncertainty in image processing of scar and grey zone. Despite the presence of some level of uncertainty, determining the ablation targets non-invasively using VAAT is shown here to be a very promising approach. Although VAAT will most probably not succeed in all patients, we are expecting it to be able to significantly raise the success rate in infarct-related VT ablation. This is similar to our approach to sudden cardiac death risk stratification, VARP¹¹; while we did not correctly predict every patient's clinical outcome, the VARP prediction was significantly (by a wide margin) better than any clinical indices used previously. Overall, should VAAT be

successfully tested in larger prospective studies, its adoption is expected to result in significant clinical benefits: (1) avoiding extensive invasive mapping to determine the ablation targets; (2) decreasing potential complications due to the short duration of the procedure; (3) using a more accurate and 3D set of targets (rather than those determined from a surface interrogation) that results in smaller ablation lesions, and (4) decreasing the number of repeated procedures, as VAAT targets incorporate those that would emerge after initial ablation.

Reporting Summary. Further information on research design is available in the Nature Research Reporting Summary linked to this article.

Code availability. The image processing software CardioViz3D can be freely obtained from <http://www.sop.inria.fr/asclepios/software/CardioViz3D>. The open-source software Seg3D used in grey-level thresholding can be obtained from <http://www.sci.utah.edu/cibc-software/seg3d.html>. Computational meshes are generated using the software Simpleware ScanIP, available from Synopsys. The ionic models are freely available from the repository CellML (<https://www.cellml.org>). Regarding the rule-based approach to assign fibre orientations in the computational mesh, the original publication¹³ presents a set of algorithms and subroutines that can be easily implemented. The electrophysiology simulator CARP has been developed by our team and used in over 60 publications; it can currently be obtained from Johns Hopkins University, the University of Bordeaux or the University of Graz. The ventricular simulations can also be executed using the open-source software CHASTE (<http://www.cs.ox.ac.uk/chaste>).

Data availability. All data supporting the findings of this study are available within the paper and its Supplementary Information. The patient MRI images used to construct the personalized heart models are available on request and on approval of Johns Hopkins Institutional Review Board. Source data for activation maps shown in Figs. 1–4 are available in figshare⁴⁴.

Received: 27 July 2017; Accepted: 27 July 2018;

Published online: 03 September 2018

References

- Stevenson, W. G. et al. Radiofrequency catheter ablation of ventricular tachycardia after myocardial infarction. *Circulation* **98**, 308–314 (1998).
- Aliot, E. M. et al. EHRA/HR expert consensus on catheter ablation of ventricular arrhythmias. *Heart Rhythm* **6**, 886–933 (2009).
- Zhong, H., Lacomis, J. M. & Schwartzman, D. On the accuracy of CartoMerge for guiding posterior left atrial ablation in man. *Heart Rhythm* **4**, 595–602 (2007).
- Brugada, J. et al. Nonsurgical transthoracic epicardial radiofrequency ablation: an alternative in incessant ventricular tachycardia. *J. Am. Coll. Cardiol.* **41**, 2036–2043 (2003).
- Sosa, E., Scanavacca, M., d'Avila, A., Oliveira, F. & Ramirez, J. A. Nonsurgical transthoracic epicardial catheter ablation to treat recurrent ventricular tachycardia occurring late after myocardial infarction. *J. Am. Coll. Cardiol.* **35**, 1442–1449 (2000).
- Dong, J. et al. Impact of heart rhythm status on registration accuracy of the left atrium for catheter ablation of atrial fibrillation. *J. Cardiovasc. Electrophysiol.* **18**, 1269–1276 (2007).
- de Bakker, J. M. et al. Reentry as a cause of ventricular tachycardia in patients with chronic ischemic heart disease: electrophysiologic and anatomic correlation. *Circulation* **77**, 589–606 (1988).
- Peters, N. S. & Wit, A. L. Myocardial architecture and ventricular arrhythmogenesis. *Circulation* **97**, 1746–1754 (1998).
- Callans, D. J. et al. Efficacy of radiofrequency catheter ablation for ventricular tachycardia in healed myocardial infarction. *Am J Cardiol* **82**, 429–432 (1998).
- Calkins, H. et al. Catheter ablation of ventricular tachycardia in patients with structural heart disease using cooled radiofrequency energy: results of a prospective multicenter study. Cooled RF Multi Center Investigators Group. *J. Am. Coll. Cardiol.* **35**, 1905–1914 (2000).
- Arevalo, H. J. et al. Arrhythmia risk stratification of patients after myocardial infarction using personalized heart models. *Nat. Commun.* **7**, 11437 (2016).
- Prakosa, A. et al. Methodology for image-based reconstruction of ventricular geometry for patient-specific modeling of cardiac electrophysiology. *Prog. Biophys. Mol. Biol.* **115**, 226–234 (2014).
- Bayer, J. D., Blake, R. C., Plank, G. & Trayanova, N. A. A novel rule-based algorithm for assigning myocardial fiber orientation to computational heart models. *Ann. Biomed. Eng.* **40**, 2243–2254 (2012).
- Zahid, S. et al. Feasibility of using patient-specific models and the "minimum cut" algorithm to predict optimal ablation targets for left atrial flutter. *Heart Rhythm* **13**, 1687–1698 (2016).
- Lardo, A. C. et al. Visualization and temporal/spatial characterization of cardiac radiofrequency ablation lesions using magnetic resonance imaging. *Circulation* **102**, 698–705 (2000).

16. Tung, R., Josephson, M. E., Reddy, V., Reynolds, M. R. & SMASH-VT Investigators. Influence of clinical and procedural predictors on ventricular tachycardia ablation outcomes: an analysis from the substrate mapping and ablation in Sinus Rhythm to Halt Ventricular Tachycardia Trial (SMASH-VT). *J. Cardiovasc. Electrophysiol.* **21**, 799–803 (2010).
17. Hsia, H. H., Lin, D., Sauer, W. H., Callans, D. J. & Marchlinski, F. E. Anatomic characterization of endocardial substrate for hemodynamically stable reentrant ventricular tachycardia: identification of endocardial conducting channels. *Heart Rhythm* **3**, 503–512 (2006).
18. Tung, R. et al. Impact of local ablation on interconnected channels within ventricular scar: mechanistic implications for substrate modification. *Circ Arrhythm Electrophysiol* **6**, 1131–1138 (2013).
19. Verma, A. et al. Relationship between successful ablation sites and the scar border zone defined by substrate mapping for ventricular tachycardia post-myocardial infarction. *J. Cardiovasc. Electrophysiol.* **16**, 465–471 (2005).
20. Krummen, D. E. et al. Modifying ventricular fibrillation by targeted rotor substrate ablation: proof-of-concept from experimental studies to clinical VF. *J. Cardiovasc. Electrophysiol.* **26**, 1117–1126 (2015).
21. Nikolov, P., Prakosa, A., Arevalo, H. J., Wu, K. C. & Trayanova, N. A novel approach to arrhythmia risk stratification in patients with non-ischemic cardiomyopathy. *Circulation* **134**, A20903–A20903 (2016).
22. Estner, H. L. et al. The critical isthmus sites of ischemic ventricular tachycardia are in zones of tissue heterogeneity, visualized by magnetic resonance imaging. *Heart Rhythm* **8**, 1942–1949 (2011).
23. Ashikaga, H. et al. Feasibility of image-based simulation to estimate ablation target in human ventricular arrhythmia. *Heart Rhythm* **10**, 1109–1116 (2013).
24. Schmidt, A. et al. Infarct tissue heterogeneity by magnetic resonance imaging identifies enhanced cardiac arrhythmia susceptibility in patients with left ventricular dysfunction. *Circulation* **115**, 2006–2014 (2007).
25. Prassl, A. J. et al. Automatically generated, anatomically accurate meshes for cardiac electrophysiology problems. *IEEE Trans. Biomed. Eng.* **56**, 1318–1330 (2009).
26. Arevalo, H., Plank, G., Helm, P., Halperin, H. & Trayanova, N. Tachycardia in post-infarction hearts: insights from 3D image-based ventricular models. *PLoS One* **8**, e68872 (2013).
27. Plank, G. et al. From mitochondrial ion channels to arrhythmias in the heart: computational techniques to bridge the spatio-temporal scales. *Phil. Trans A Math. Phys. Eng. Sci.* **366**, 3381–3409 (2008).
28. Gurev, V., Lee, T., Constantino, J., Arevalo, H. & Trayanova, N. A. Models of cardiac electromechanics based on individual hearts imaging data: image-based electromechanical models of the heart. *Biomech. Model. Mechanobiol.* **10**, 295–306 (2011).
29. Deng, D. et al. Accuracy of prediction of infarct-related arrhythmic circuits from image-based models reconstructed from low and high resolution MRI. *Front. Physiol.* **6**, 282 (2015).
30. Pashkhanloo, F. et al. Submillimeter diffusion tensor imaging and late gadolinium enhancement cardiovascular magnetic resonance of chronic myocardial infarction. *J. Cardiovasc. Magn. Reson.* **19**, 9 (2017).
31. Ten Tusscher, K. H., Noble, D., Noble, P. J. & Panfilov, A. V. A model for human ventricular tissue. *Am. J. Physiol. Heart Circ. Physiol.* **286**, H1573–H1589 (2004).
32. Decker, K. F. & Rudy, Y. Ionic mechanisms of electrophysiological heterogeneity and conduction block in the infarct border zone. *Am. J. Physiol. Heart Circ. Physiol.* **299**, H1588–H1597 (2010).
33. Cabo, C. & Boyden, P. A. Electrical remodeling of the epicardial border zone in the canine infarcted heart: a computational analysis. *Am. J. Physiol. Heart Circ. Physiol.* **284**, H372–H384 (2003).
34. Vigmond, E. J., Weber dos Santos, R., Prassl, A. J., Deo, M. & Plank, G. Solvers for the cardiac bidomain equations. *Prog. Biophys. Mol. Biol.* **96**, 3–18 (2008).
35. Rodriguez, B., Li, L., Eason, J. C., Efimov, I. R. & Trayanova, N. A. Differences between left and right ventricular chamber geometry affect cardiac vulnerability to electric shocks. *Circ. Res.* **97**, 168–175 (2005).
36. Rantner, L. J. et al. Three-dimensional mechanisms of increased vulnerability to electric shocks in myocardial infarction: altered virtual electrode polarizations and conduction delay in the peri-infarct zone. *J. Physiol.* **590**, 4537–4551 (2012).
37. Bishop, M. J. et al. The role of photon scattering in optical signal distortion during arrhythmia and defibrillation. *Biophys. J.* **93**, 3714–3726 (2007).
38. Cerqueira, M. D. et al. Standardized myocardial segmentation and nomenclature for tomographic imaging of the heart. A statement for healthcare professionals from the Cardiac Imaging Committee of the Council on Clinical Cardiology of the American Heart Association. *Circulation* **105**, 539–542 (2002).
39. Piccini, J. P. et al. Mode of induction of ventricular tachycardia and prognosis in patients with coronary disease: the Multicenter UnSustained Tachycardia Trial (MUSTT). *J. Cardiovasc. Electrophysiol.* **20**, 850–855 (2009).
40. Buxton, A. E. Programmed ventricular stimulation: not dead. *Circulation* **129**, 831–833 (2014).
41. Vadakkumpadan, F., Trayanova, N. & Wu, K. C. Image-based left ventricular shape analysis for sudden cardiac death risk stratification. *Heart Rhythm* **11**, 1693–1700 (2014).
42. Ranjan, R. et al. Personalized MRI-based modeling predicts ventricular tachycardia vulnerability in patients receiving primary prevention ICDs. *Circulation* **134**, A16247–A16247 (2016).
43. Boykov, Y. & Kolmogorov, V. An experimental comparison of min-cut/max-flow algorithms for energy minimization in vision. *IEEE Trans. Pattern Anal. Mach. Intell.* **26**, 1124–1137 (2004).
44. Prakosa, A. et al. Dataset for Personalized virtual-heart technology for guiding the ablation of infarct-related ventricular tachycardia. *figshare* <https://doi.org/10.6084/m9.figshare.6613289> (2018).

Acknowledgements

This work was supported by the NIH Pioneer Award (DP1-HL123271) to N.A.T.

Author contributions

A.P., H.J.A., D.D., H.A. and P.P.N. performed animal and human LGE-MRI scan segmentation and model creation. A.P., H.J.A., D.D. and N.A.T. designed the simulation protocols. D.D., H.J.A., A.P. and P.N. performed simulations of VT in all models. D.D., A.P., P.M.B., H.J.A. and N.A.T. analysed the data. A.P. developed the pipeline for model generation from MRI scans with ICD artefact. D.D. and A.P. adapted the automatic algorithm for determining the ablation targets in the ventricles. H.H. provided the swine MRI and electrophysiological data, as well as input for the animal study. S.N. provided part of the human MRI scans (at Johns Hopkins), conducted the prospective studies at the University of Pennsylvania, and provided clinical guidance and input. J.C. provided the remainder of the human MRI scans and patient outcomes. A.P. developed the methodology for input of simulation data into the clinical CARTO mapping system. J.B., E.G., R.M. and R.R. developed and implemented the clinical protocols at the University of Utah. R.R. and F.H. recruited patients and conducted VT ablations for the prospective human study at the University of Utah. S.N. and D.C. recruited patients and conducted VT ablations for the prospective human study at the University of Pennsylvania. N.A.T. initiated the collaborations, designed and coordinated the studies with contributions from H.J.A. and H.H. (retrospective swine and human studies), S.N. and R.R. (prospective human studies), and A.P. and S.N. (retrospective human with ICD study), and supervised all simulation studies. H.J.A., D.D., A.P., P.M.B., E.G. and R.R. generated figures, tables and videos. N.A.T. wrote the manuscript with input from A.P. and H.J.A. All authors discussed the results and commented on the manuscript.

Competing interests

N.A.T. holds partial ownership of CardioSolv Ablation Technologies LLC. S.N. is a scientific advisor to CardioSolv Ablation Technologies LLC. The other authors declare no competing interests.

Additional information

Supplementary information is available for this paper at <https://doi.org/10.1038/s41551-018-0282-2>.



Reprints and permissions information is available at www.nature.com/reprints.

Correspondence and requests for materials should be addressed to N.A.T.

Publisher's note: Springer Nature remains neutral with regard to jurisdictional claims in published maps and institutional affiliations.

In the format provided by the authors and unedited.

Personalized virtual-heart technology for guiding the ablation of infarct-related ventricular tachycardia

Adityo Prakosa^{1,7}, Hermenegild J. Arevalo^{1,2,7}, Dongdong Deng^{1,7}, Patrick M. Boyle ¹, Plamen P. Nikolov¹, Hiroshi Ashikaga³, Joshua J. E. Blauer⁴, Elyar Ghafoori⁴, Carolyn J. Park¹, Robert C. Blake III¹, Frederick T. Han⁵, Rob S. MacLeod ⁴, Henry R. Halperin³, David J. Callans⁶, Ravi Ranjan⁴, Jonathan Chrispin³, Saman Nazarian⁶ and Natalia A. Trayanova^{1,3*}

¹Institute for Computational Medicine and Department of Biomedical Engineering, Johns Hopkins University, Baltimore, MD, USA. ²Cardiac Modelling Department, Simula Research Laboratory, Fornebu, Norway. ³Division of Cardiology, Department of Medicine, Johns Hopkins University School of Medicine, Baltimore, MD, USA. ⁴Department of Bioengineering, University of Utah, Salt Lake City, UT, USA. ⁵University of Utah Health Sciences Center, Salt Lake City, UT, USA. ⁶Department of Medicine, University of Pennsylvania, Philadelphia, PA, USA. ⁷These authors contributed equally: Adityo Prakosa, Hermenegild J. Arevalo, Dongdong Deng. *e-mail: ntrayanova@jhu.edu

Supplementary Information

Table of Contents

| | |
|--|----------|
| Supplementary Tables | 2 |
| <i>Supplementary Table 1: VAAT lesion sizes in swine study</i> | <i>2</i> |
| <i>Supplementary Table 2: VAAT total volume of the ablation lesions in retrospective human study</i> | <i>2</i> |
| <i>Supplementary Table 3: VAAT details from study of patients with ICDs</i> | <i>2</i> |
| Supplementary Figures | 3 |
| <i>Supplementary Figure 1: Additional results from retrospective swine studies.....</i> | <i>3</i> |
| <i>Supplementary Figure 2: Additional results from retrospective human studies.....</i> | <i>4</i> |
| <i>Supplementary Figure 3: Model reconstruction method for patients with ICDs.....</i> | <i>5</i> |
| <i>Supplementary Figure 4: Additional results from study of patients with ICDs</i> | <i>6</i> |
| <i>Supplementary Figure 5: VT model from Utah prospective human study</i> | <i>7</i> |
| Captions for Supplementary Movies | 7 |

Supplementary Table 1: VAAT lesion sizes in swine where experimental mapping-based ablation failed to terminate VT.

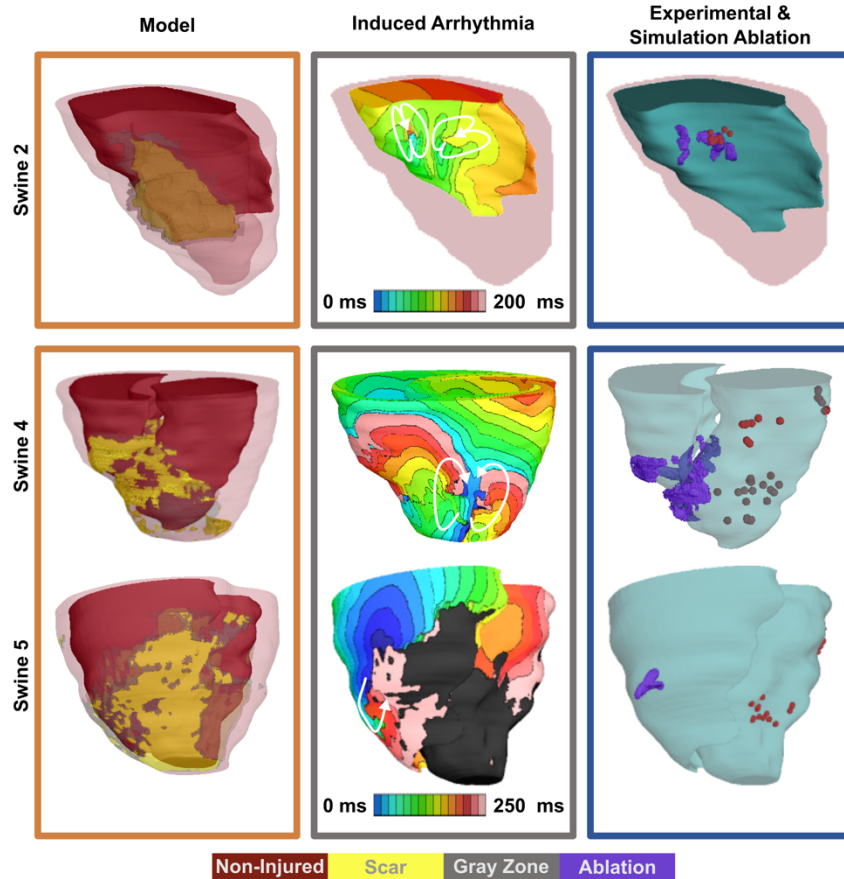
| Swine | Ablation size (cm³) |
|--------------|---------------------------------------|
| 3 | 0.15 |
| 4 | 2.25 |
| 5 | 0.13 |

Supplementary Table 2: VAAT total volume of the ablation lesions in the retrospective human study (n = 16).

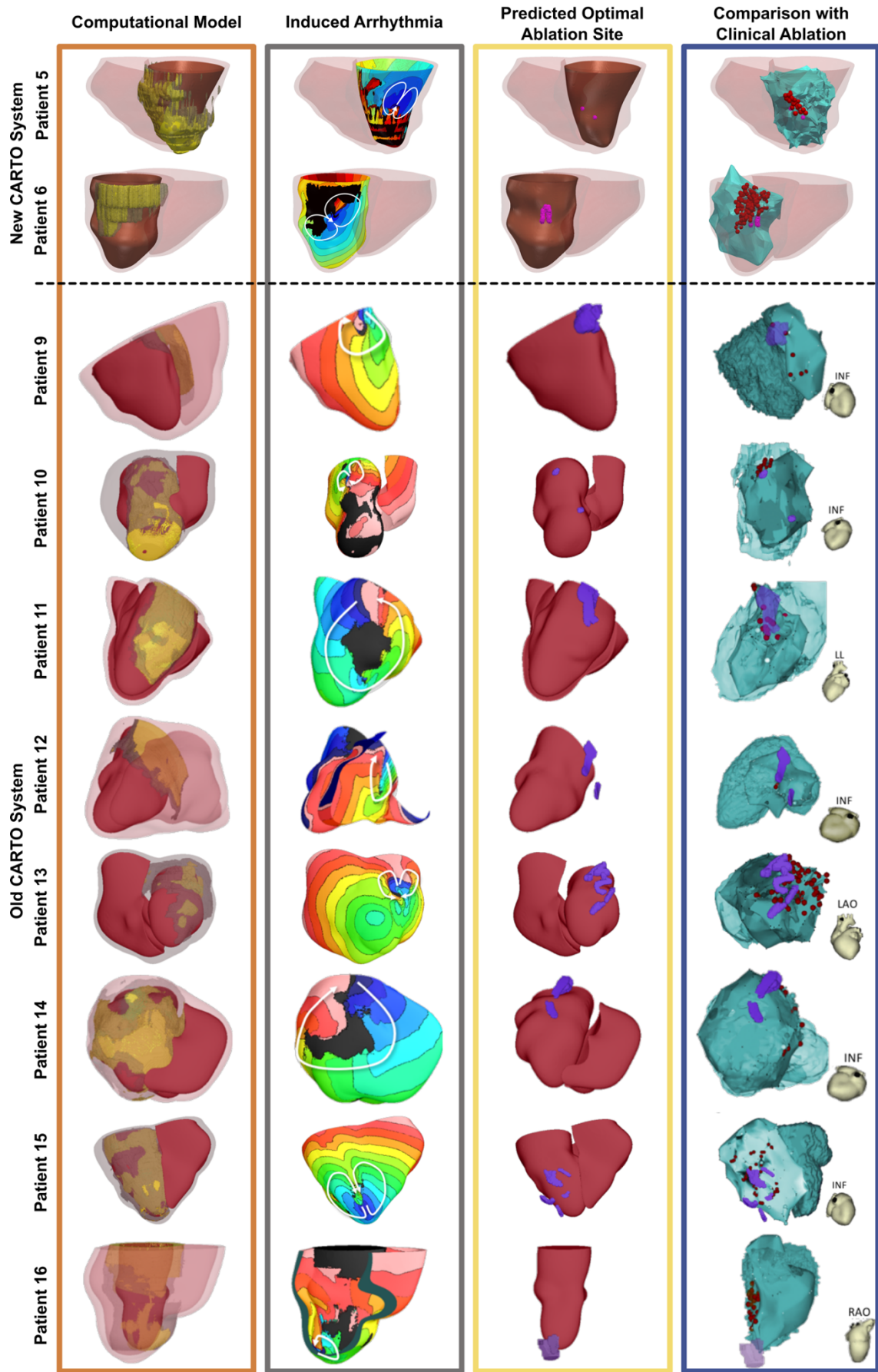
| Patient | Ablation size (cm³) |
|----------------|---------------------------------------|
| 1 | 0.10 |
| 2 | 0.22 |
| 3 | 0.10 |
| 4 | 0.72 |
| 5 | 0.52 |
| 6 | 0.71 |
| 7 | 0.53 |
| 8 | 0.56 |
| 9 | 2.52 |
| 10 | 0.16 |
| 11 | 2.00 |
| 12 | 0.64 |
| 13 | 1.98 |
| 14 | 1.57 |
| 15 | 1.56 |
| 16 | 2.61 |

Supplementary Table 3: Myocardial wall artefact burdens and VAAT lesion sizes in the retrospective human study involving patients with ICDs (n = 5).

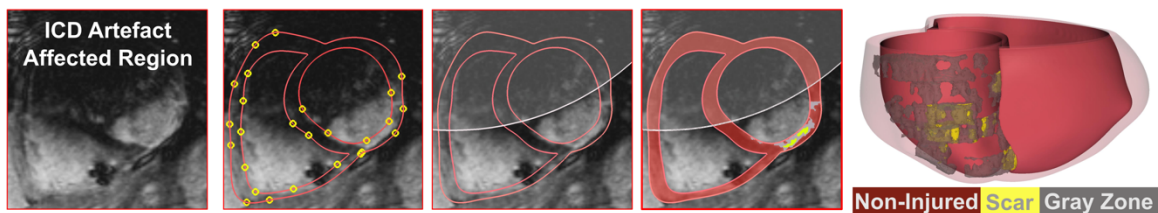
| Patient | Artefact Burden | Ablation size (cm³) |
|----------------|------------------------|---------------------------------------|
| 1 | 59% | 0.31 |
| 2 | 46% | 0.36 |
| 3 | 1% | 0.68 |
| 4 | 0% | 0.79 |
| 5 | 62% | 0.17 |



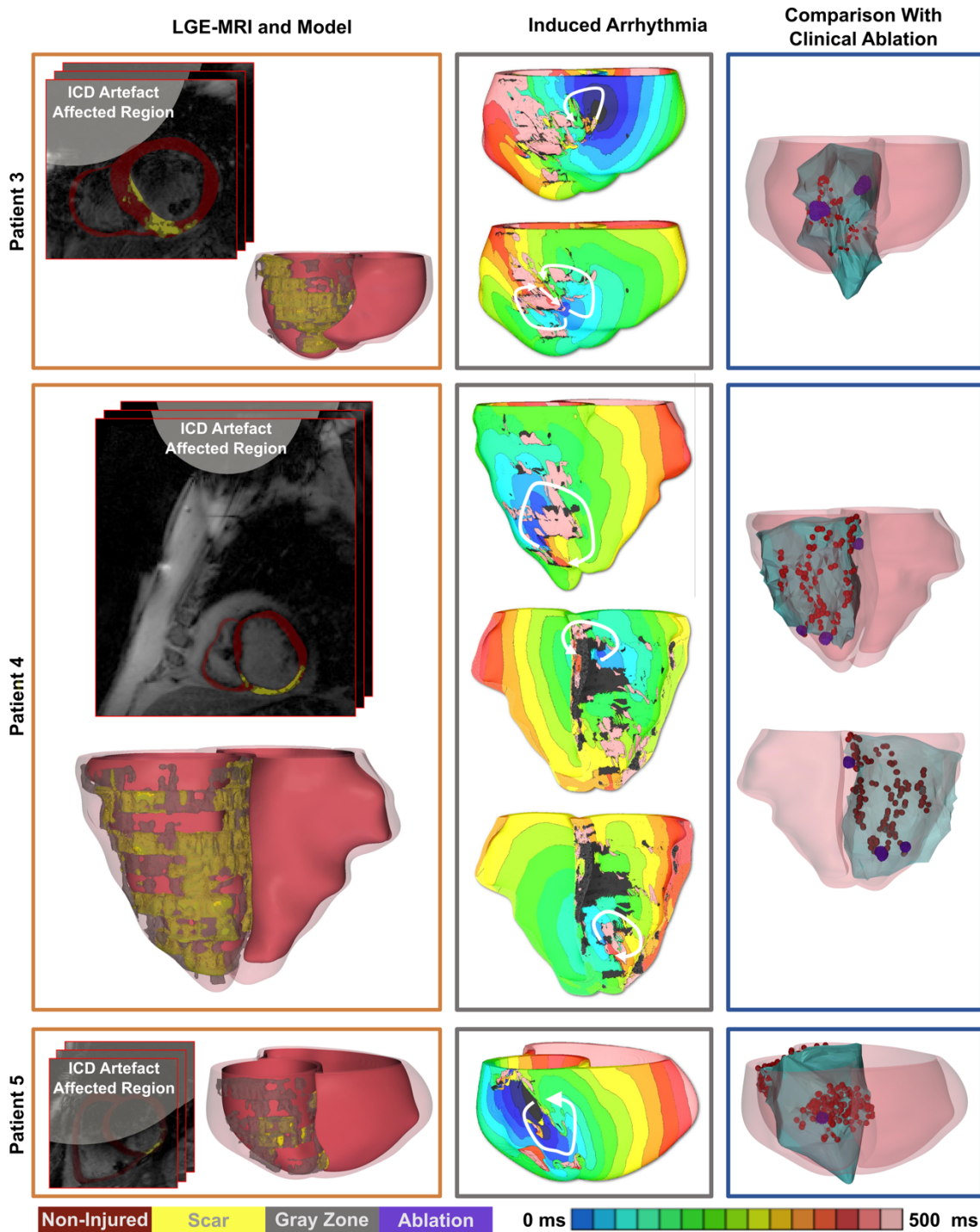
Supplementary Figure 1: VAAT prediction: results from the remaining 3 swine hearts in the animal study. Illustrated are one case of successful (Swine 2) and two cases of failed (Swine 4 and 5) mapping-guided ablation and the respective models and VAAT predictions. Image frame colours correspond to the steps outlined in Fig. 1a. Panels present, from left to right: reconstructed ventricular models with different remodelled regions; endocardial (Swine 2) or epicardial (Swine 4 and 5) electrical activation maps of the infarct-related VTs and arrows showing direction of propagation; VAAT predicted ablation targets (purple) on the ventricular endocardial (Swine 2) or epicardial (Swine 4 and 5) surface; and comparison of these with experimental mapping-based endocardial ablation locations. In the latter images, red dots represent locations of the tip of the catheter during ablation; to depict those, ventricular geometry from post-ablation CT scans was co-registered with the MRI-based model. Note that in Swine 2, VAAT predicted that two VT reentrant circuits could be sustained by the ventricular substrate. Only one of these was manifested in the animal during the procedure, and the corresponding target ablated. Identifying all possible VT circuits that can be sustained in a given substrate, and not only those manifested or induced at the time of procedure is an advantage of our approach since it could decrease or even eliminate the need for repeated ablations.



Supplementary Figure 2 (previous page): *Results from additional 10 patient heart models in the retrospective human study.* Image frame colours correspond to the steps outlined in Fig. 1a. The top 2 patients were ablated using a newer version of the CARTO electroanatomical navigation system, the same used for the results shown in Fig. 2. The remaining 8 patients were ablated using an older version of the CARTO system. Panels present, from left to right: reconstructed ventricular models with different structurally-remodelled regions; electrical activation maps of the infarct-related VTs on the epi- or endocardial surfaces (chosen for best visualization) and arrows showing direction of propagation; VAAT predicted ablation targets (purple) on the endocardial surface; and co-registration of the VAAT targets with the CARTO endocardial surface (green) showing clinical ablation locations (red dots represent locations of the tip of the catheter during ablation). Small hearts at bottom left show heart orientation in the older CARTO system (LAO = left anterior oblique, RAO = right anterior oblique, and INF = inferior view).

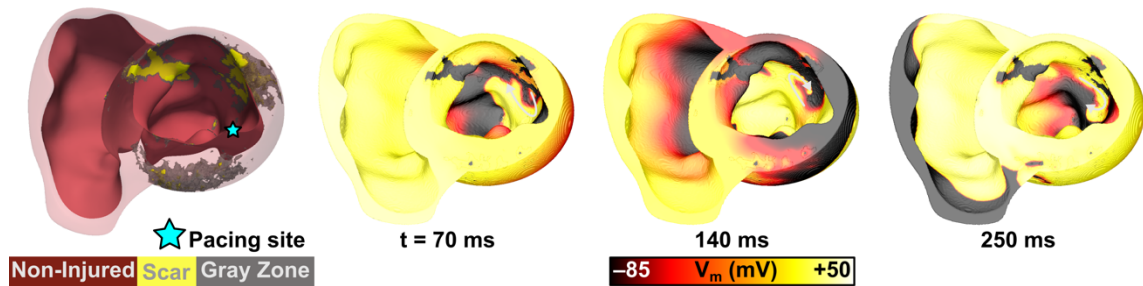


Supplementary Figure 3: *Ventricular model construction from LGE MRI scans with ICD artefact burden.* Panels present, from left to right: LGE MRI scans with ICD artefact burden; ventricular myocardial wall segmentation relying on the prominent boundaries of the visible myocardial wall and extrapolation into areas covered by the artefact; delineation of ICD artefact in the ventricular myocardium based on the 3D radial distance from the ICD; myocardial tissue classification; and resulting ventricular model.



Supplementary Figure 4: Results from the remaining 3 human heart models in the retrospective study in patients with ICDs. Panel frame colours corresponds to Fig. 1a. Panels present, from left to right: LGE-MRI scans with ICD artefact burden and reconstructed ventricular models with different remodelled regions; electrical

activation maps of the infarct-related VTs on the epicardial surfaces and arrows showing direction of VT propagation; and co-registration of ventricular model surfaces and VAAT-predicted ablation targets with the CARTO endocardial surface (green) showing clinical ablation locations (red dots representing locations of the tip of the catheter during ablation). In patients 3 and 4, the ICD artefact did not cover the myocardial wall. In patient 5, the ICD artefact covered 62% of the myocardial wall. In all cases, VAAT-predicted targets were located within the areas ablated clinically. In Patient 5, there was an additional clinical ablation on the anterior LV wall that was not predicted by the simulations since that part of the ventricular wall was covered by the ICD artefact. In such severe cases, non-invasive ablation target prediction can only partially substitute electrical mapping. We expect that in such cases, in the clinical implementation the predicted targets will be first ablated, and if VT remains inducible, then mapping can be used to determine the remaining ablation target(s) that the simulations could not reveal.



Supplementary Figure 5: *Initiation of sustained VT in the heart model of the patient from the prospective human study at the University of Utah (corresponding to one of the VT morphologies in Fig. 4b)* . Shown are patient heart geometry and transmembrane potential maps of one of the induced VTs in this patient at three time instants. White arrows show direction of propagation. Time below each map is counted from the delivery of the last pacing stimulus. Propagation through a channel in the scar is visible. See also Supplementary Movie 2.

Supplementary Movie 1: Initiation of VT for patient 2 in the retrospective human study of patients with ICDs. The movie starts at 300 ms after the delivery of the sixth S1 ($t = 2550$ ms) and shows the subsequent delivery of S2 ($t = 2570$ ms) and S3 ($t = 2800$ ms), and then 2000-ms period of induced VT. Note wavefront propagation through patchy infarct areas.

Supplementary Movie 2: Initiation of sustained VT in the heart model of the patient from the prospective human study at the University of Utah (corresponding to one of the VT morphologies in Fig. 4b, and to Supplementary Figure 5).

Reporting Summary

Nature Research wishes to improve the reproducibility of the work that we publish. This form provides structure for consistency and transparency in reporting. For further information on Nature Research policies, see [Authors & Referees](#) and the [Editorial Policy Checklist](#).

Statistical parameters

When statistical analyses are reported, confirm that the following items are present in the relevant location (e.g. figure legend, table legend, main text, or Methods section).

n/a | Confirmed

- The exact sample size (n) for each experimental group/condition, given as a discrete number and unit of measurement
- An indication of whether measurements were taken from distinct samples or whether the same sample was measured repeatedly
- The statistical test(s) used AND whether they are one- or two-sided
Only common tests should be described solely by name; describe more complex techniques in the Methods section.
- A description of all covariates tested
- A description of any assumptions or corrections, such as tests of normality and adjustment for multiple comparisons
- A full description of the statistics including central tendency (e.g. means) or other basic estimates (e.g. regression coefficient) AND variation (e.g. standard deviation) or associated estimates of uncertainty (e.g. confidence intervals)
- For null hypothesis testing, the test statistic (e.g. F , t , r) with confidence intervals, effect sizes, degrees of freedom and P value noted
Give P values as exact values whenever suitable.
- For Bayesian analysis, information on the choice of priors and Markov chain Monte Carlo settings
- For hierarchical and complex designs, identification of the appropriate level for tests and full reporting of outcomes
- Estimates of effect sizes (e.g. Cohen's d , Pearson's r), indicating how they were calculated
- Clearly defined error bars
State explicitly what error bars represent (e.g. SD, SE, CI)

Our web collection on [statistics for biologists](#) may be useful.

Software and code

Policy information about [availability of computer code](#)

Data collection

No software was used in the data-collection component of this study.

Data analysis

The software CARP (ver. 1.8.1) was used to perform all simulations. This software has been extensively used and tested by our group and others. A free version of this software (CARPentry) can be downloaded for academic use at <https://carp.medunigraz.at/carputils/>. The image-processing software, CardioViz3D (ver. 1.5), can be freely obtained from <http://www-sop.inria.fr/asclepios/software/CardioViz3D/>. The open-source software Seg3D (ver. 2.4.1) used in gray-level thresholding can be obtained from <http://www.sci.utah.edu/cibc-software/seg3d.html>. Computational meshes are generated using the software Simpleware ScanIP (ver. 7), available from Synopsys. The ionic models are freely available from the repository CellML (<https://www.cellml.org/>). The ventricular simulations can also be executed using the open-source software CHASTE: <http://www.cs.ox.ac.uk/chaste/>.

For manuscripts utilizing custom algorithms or software that are central to the research but not yet described in published literature, software must be made available to editors/reviewers upon request. We strongly encourage code deposition in a community repository (e.g. GitHub). See the Nature Research [guidelines for submitting code & software](#) for further information.

Data

Policy information about [availability of data](#)

All manuscripts must include a [data availability statement](#). This statement should provide the following information, where applicable:

- Accession codes, unique identifiers, or web links for publicly available datasets
- A list of figures that have associated raw data
- A description of any restrictions on data availability

Relevant data, including patient MRI scans, are available from the authors upon approval of the Johns Hopkins Institutional Review Board; other than IRB approval, there are no specific restrictions on the availability of the materials used in the study. Source data for activation maps shown in Figs. 1–4 are available in figshare, with the identifier doi:10.6084/m9.figshare.6613289. No antibodies or eukaryotic cell lines were used in this study.

Field-specific reporting

Please select the best fit for your research. If you are not sure, read the appropriate sections before making your selection.

Life sciences Behavioural & social sciences Ecological, evolutionary & environmental sciences

For a reference copy of the document with all sections, see [nature.com/authors/policies/ReportingSummary-flat.pdf](https://www.nature.com/authors/policies/ReportingSummary-flat.pdf)

Life sciences study design

All studies must disclose on these points even when the disclosure is negative.

| | |
|-----------------|--|
| Sample size | The number of subjects available for the study was limited by the available experimental and clinical data. (1) Retrospective pig study – All 5 pigs for which experimental data was collected in [22] were used in this simulation study. (2) Retrospective human study – 21 patient-specific heart models, from patients that underwent clinical ablation were used in this study. Of those, 16 were without ICDs and 5 were with ICDs. The patient clinical LGE-MRI scans were of sufficient quality to construct a virtual heart model. (3) Prospective human study – A prospective study of 5 patients was conducted, at two different clinical centers. Of these 3 were enrolled in the study at the University of Utah and 2 were enrolled at the University of Pennsylvania. The MRI scans were of sufficient quality to construct a model. |
| Data exclusions | All data generated are presented in the study. |
| Replication | The numerical stability and reproducibility of the software CARP has been thoroughly tested by our group. Since all models are deterministic, simulation results would be the same when repeated. |
| Randomization | Not applicable because this is a pilot study, not a randomized clinical trial. |
| Blinding | In the prospective study, the team performing the simulations were only given the patient MRI. No other clinical information was available. In the retrospective patient with and without ICD study, the simulation team was blinded to patient clinical information and outcomes. |

Reporting for specific materials, systems and methods

Materials & experimental systems

| n/a | Involvement |
|-------------------------------------|---|
| <input checked="" type="checkbox"/> | <input type="checkbox"/> Unique biological materials |
| <input checked="" type="checkbox"/> | <input type="checkbox"/> Antibodies |
| <input checked="" type="checkbox"/> | <input type="checkbox"/> Eukaryotic cell lines |
| <input checked="" type="checkbox"/> | <input type="checkbox"/> Palaeontology |
| <input type="checkbox"/> | <input checked="" type="checkbox"/> Animals and other organisms |
| <input type="checkbox"/> | <input checked="" type="checkbox"/> Human research participants |

Methods

| n/a | Involvement |
|-------------------------------------|---|
| <input checked="" type="checkbox"/> | <input type="checkbox"/> ChIP-seq |
| <input checked="" type="checkbox"/> | <input type="checkbox"/> Flow cytometry |
| <input checked="" type="checkbox"/> | <input type="checkbox"/> MRI-based neuroimaging |

Animals and other organisms

Policy information about [studies involving animals](#); [ARRIVE guidelines](#) recommended for reporting animal research

| | |
|-------------------------|---|
| Laboratory animals | Details on the animals can be found in reference [22]. Domestic swine were studied with an occlusion of their mid-left anterior descending coronary artery. All animals were ~2 months old, with weights ranging 18–23 kg, and 2/5 were male. |
| Wild animals | The study did not involve wild animals. |
| Field-collected samples | The study did not involve samples collected from the field. |

Human research participants

Policy information about [studies involving human research participants](#)

| | |
|----------------------------|---|
| Population characteristics | <p>All human participants had ischemic cardiomyopathy and presented with clinical ventricular tachycardia. All human participants had LGE-MRI scans of sufficient quality to construct a virtual heart model. Covariate-relevant population characteristics of the participants for the different sub-studies were as follows:</p> <ol style="list-style-type: none"> 1) Retrospective study #1: mean age 64.4±9 y, mean LVEF 38.4±12%, 87.5% male 2) Retrospective study #2: mean age 64.1±15.5 y, mean LVEF 31.1±16.4, 75% male 3) Retrospective study of patients with ICDs: mean age 54.2±9.3 y, mean LVEF 39±13.8%, 100% male 4A) Prospective study (University of Utah cohort): mean age 66.6±9.9 y, mean LVEF 40±6.6%, 2/3 male 4B) Prospective study (University of Pennsylvania cohort): mean age 73.5±3.4 y, mean LVEF 33±4.4%, 2/2 male |
| Recruitment | The number of subjects available for the study was limited by the available clinical data. |